Electrochimica Acta 480 (2024) 143933

Contents lists available at ScienceDirect

Electrochimica Acta

journal homepage: www.journals.elsevier.com/electrochimica-acta

Reconstructing 2D metallic Sn_4P_3 with high-conductive interlayer towards high-rate lithium storage

Jianan Gu, Yanlong Lv, Yanhong Wang, Lehao Liu, Meicheng Li *

State Key Laboratory of Alternate Electrical Power System with Renewable Energy Sources, School of New Energy, North China Electric Power University, 100096 Beijing, China

ARTICLE INFO

Keywords:
2D materials
Sn_4P_3 layers
High-conductive interlayer
High-rate
Lithium ion batteries

ABSTRACT

Lithium-ion batteries are extensively utilized in various applications but face challenges in terms of anode performance. Commercial graphite possesses a low theoretical capacity of mAh g^{-1}, which falls short of the desired performance. Alternatively, tin phosphide (Sn_4P_3) possesses a remarkable theoretical capacity of 1230 mAh g^{-1}, making it a highly promising candidate. However, Sn_4P_3, being a semiconductor, faces challenges such as poor conductivity as well as substantial volume expansions during the lithiation–delithiation process. Herein, we fabricated a 2D Sn_4P_3 nanocomposite with high-conductive-interlayer *via* a breaking-reconstructing strategy. In this process, the 2D Sn_4P_3 layers were first achieved by a liquid-exfoliation method, revealing their unique metallic properties by density-functional-theory calculations. Besides, the 2D conductive-interlayer Sn_4P_3 demonstrated good electrochemical performance, including high reversible capacity, stable cyclic life, and high-rate capabilities. Alternating current impedance spectroscopy analysis further revealed that low charge-transfer resistance and a high lithium ion diffusion coefficient, contributing to the enhanced electrochemical performance. These findings demonstrate the significance of exfoliating Sn_4P_3 into layered structures and highlight the potential of 2D conductive-interlayer Sn_4P_3 nanocomposites as promising candidates for high-performance anodes.

1. Introduction

Lithium-ion batteries (LIBs) play an important role in diverse applications, including electric vehicles, portable electronics, and electrical storage stations. [1–7] However, as the current anode material, commercial graphite falls short of meeting the performance requirements of LIBs because of its limited capacity of 372 mAh g^{-1} in theory [8–12]. This has spurred significant efforts to explore new anode materials with higher capacities, superior rate performance, and longer cycle life [13–17].

Among the various types of lithium storage mechanisms, conversion mechanism-based electrodes, including oxides, sulfides, as well as phosphides, have shown promising theoretical capacities compared to traditional carbon-based materials that operate through intercalation mechanisms [18–23]. In particular, phosphides offer lower and suitable potential voltages for lithium storage, which are significantly higher than the voltage required for lithium deposition [24–28]. This characteristic decreases the danger of Li dendrite formation and enhances safety, especially during overcharging. Additionally, phosphides exhibit substantially higher theoretical capacities compared to oxides and sulfides [29–33]. For instance, tin phosphide (Sn_4P_3) possesses a remarkable theoretical capacity of 1230 mAh g^{-1}, surpassing tin dioxide (SnO_2: 790 mAh g^{-1}) as well as tin bisulfide (SnS_2: 645 mAh g^{-1}) [34–36].

However, phosphides face certain challenges, including lower electrical conductivity and significant volume changes during the discharge/charge process, resulting in a loss of electrical contact as well as rapid capacity decay [37–41]. To address these issues, several methods have been proposed, such as constructing zero-dimensional (0D) Sn_4P_3/C core–shell structures, [42] three-dimensional (3D) graphene/Ni_2P hybrid, [43] and Mn-doped Sn_4P_3 nanoparticles [44]. While these methods relieved the volume expansion during the lithiation/delithiation process, achieving the full potential of high theoretical capacities remains a challenge, leaving ample room for improvement in capacities, rate performance, and long cycle life.

Herein, we address these challenges by introducing a novel strategy for fabricating a 2D Sn_4P_3 nanocomposite with a high-conductive interlayer. Through a breaking-reconstructing process, ultrathin 2D Sn_4P_3 layers are first achieved using a liquid-exfoliation method,

* Corresponding author.
E-mail address: mcli@ncepu.edu.cn (M. Li).

https://doi.org/10.1016/j.electacta.2024.143933
Received 21 December 2023; Received in revised form 24 January 2024; Accepted 8 February 2024
Available online 9 February 2024

showcasing their distinctive metallic properties as elucidated by density-functional-theory calculations. Besides, the 2D conductive-interlayer Sn_4P_3 demonstrated good electrochemical performance, such as high reversible capacity, stable cyclic life, and high-rate properties. Alternating current (AC) impedance spectroscopy analysis further revealed that a high Li^+ diffusion coefficient, contributing to the enhanced electrochemical performance. The incorporation of conductive carbon layer further improved stability and lithium ion transport properties. These findings demonstrate the significance of exfoliating Sn_4P_3 into 2D layers and highlight the potential of 2D conductive-interlayer Sn_4P_3 nanocomposites as promising candidates for high-performance anodes of LIBs.

2. Experimental

2.1. The synthesis of 2D Sn_4P_3 layers

Bulk Sn_4P_3 powders were initially suspended in various solvents, including IPA, NMP, and DMF, to generate a separate dispersions with consistent concentration (2 mg mL^{-1}). Subsequently, these dispersions were subjected to sonication under ambient conditions, inducing the gradual exfoliation of the bulk Sn_4P_3 into few-layer Sn_4P_3 nanosheets, with the extent of exfoliation increasing with sonication time. For instance, a quantity of 100 mg of bulk Sn_4P_3 powders was introduced into 50 ml of IPA solvent, pre-saturated with argon (Ar) gas, followed by ultrasonication for a duration of 20 h. Subsequent to this treatment, the resultant products underwent thorough washing with deionized water and ethanol on multiple occasions.

2.2. The synthesis of 2D high-conductive-interlayer Sn_4P_3 layers

Solution A: Dissolve 100 mg of glucose in 80 mL of H_2O. Solution B: Disperse 160 mg of 2D Sn_4P_3 layers in 80 mL of H_2O. Gradually add Solution A into Solution B with stirring. Once added, heat the solution to 180 °C for 12 h by a hydrothermal reaction. Subsequently, pyrolyze the mixture under an Ar atmosphere at 500 °C. The resulting product is then dispersed in 100 mL of H_2O for sonication and subsequently filtered under vacuum to form the 2D stacked layers.

2.3. Eletrochemical measurements

In 2032 coin-type cells, electrochemical experiments were conducted. The working electrodes were fabricated by blending active materials, carbon black, and PVDF at a weight ratio of 7:2:1. This mixture was then applied onto pure copper foil and dried at 120 °C under vacuum for 12 h. The mass loading of active materials was ~ 0.84 mg cm^{-2}. The counter electrode utilized pure lithium foil. The electrolyte consisted of a 1 M $LiClO_4$ solution in propylene carbonate, and a PP film served as the separator. Assembly of the cells took place in an Ar-filled glove box with moisture and oxygen concentrations kept below 0.1 ppm. Charge and discharge measurements were conducted using the Land CT2001A system at different rates (74.4, 168, 372, 744, 1680, and 3720 mA g^{-1}). Electrochemical performance was evaluated at different current densities within the voltage range of 0.01–3.00 V. Electrochemical impedance spectroscopy (EIS) measurements were carried out using Autolab equipment (PGSTAT302N). Impedance spectra were recorded by applying a sine wave with an amplitude of 5.0 mV across the frequency range from 100 kHz to 0.01 Hz. Fitting of the impedance spectra to the proposed equivalent circuit was performed using the Zview software.

2.4. Calculation of exchange current density

The exchange current density in active materials can be calculated using the equation of $J = RT/nFR_{ct}$, where R is the gas constant (8.314 J mol^{-1} k^{-1}), T is the temperature (298 K), n is the number of electrons, F is the Faraday constant (96485 C mol^{-1}), and R is the charge-transfer resistance.

2.5. Calculation of diffusion coefficient of lithium ion

The Warburg factor (σ_w) is related to the mass transport, obtained from the slope between Z_{re} and $\omega^{-1/2}$, as shown in Fig. 5b in main text. From this value, the Li^+ diffusion coefficient in the active material can be calculated based on the equation of $R^2T^2/2A^2n^4F^4C^2\sigma_w^2$, where R is the gas constant (8.314 J mol^{-1} k^{-1}), T is the temperature (298 K), A is the surface area of the electrode (l.13 cm^{-2}), n is the number of electrons, F is the Faraday constant (96,485 C mol^{-1}), and C is the molar concentration of Li.

2.6. Calculation of binding energy and PDOS

To compute the binding energy, the algorithm operates under the assumption that the interlayer energy profile forms a single-valley curve. It systematically seeks the minimum, ensuring that each step results in a reduction of either energy or force. Upon convergence, the algorithm provides the maximum binding energy (Eb) at the equilibrium distance (d0). Simultaneously, the critical binding force (Fb) is determined at the critical distance (d1). This algorithm has been implemented in Python to ensure compatibility with VASP.

The Sn_4P_3 layer calculations were carried out employing the projector augmented wave (PAW) method, utilizing the Perdew–Burke–Ernzerhof (PBE) generalized gradient approximation (GGA) functional, and incorporating the Heyd–Scuseria–Ernzerhof (HSE) hybrid functional, a recent addition to the VASP code. The geometrical structures were derived from experimental XRD measurements, and the energy cutoff for the plane-wave basis expansion was set to 500 eV. Total energies were computed using both PBE and HSE functionals, with a convergence criterion set at 1×10^{-5} eV per unit cell. For the partial density of states (PDOS) calculations, a denser k-points grid of $8 \times 8 \times 1$ was employed.

3. Results and discussion

The synthesis process for 2D high-conductive-interlayer Sn_4P_3 mainly involved three steps (Fig. 1). Initially, the 2D Sn_4P_3 layer was prepared through a liquid-exfoliation process, which involved the exfoliation of the Sn_4P_3 bulk. Subsequently, the conductive carbon layer was linked to the surface of 2D Sn_4P_3 layers by the pyrolysis process. Finally, the 2D high-conductive-interlayer Sn_4P_3 was assembled using a 2D stacking strategy (See experimental section).

In the process, Sn_4P_3 bulk was first synthesized by a facile solvothermal method (Fig. S1). Typically, a mixture of tin (Sn) powders and amorphous red phosphorous (P) powders underwent hydrothermal treatment at 200 °C for 40 h in ethylenediamine solvent under inert conditions. The resulting powders were then immersed into aqueous HCl solution and collected by centrifugation (For more detailed, see experimental section and supporting information). Then, X-Ray Diffraction (XRD) measurements were subsequently performed to validate the crystalline structure of the resulting Sn_4P_3 samples. The XRD spectra, as illustrated in Fig. S2, exhibited consistency with the standard PDF card of Sn_4P_3 at the peak positions. This correspondence unequivocally demonstrates the successful synthesis of Sn_4P_3 bulk without any impurities.

In contrast to other phosphides, Sn_4P_3 has been relatively overlooked as a 2D material. However, it should be noted that Sn_4P_3 is inherently a layered material with a hexagonal crystal structure, belonging to the space group ($R\bar{3}m$) with lattice parameters of $a = 3.97$ Å and $c = 35.33$ Å. [45] This crystal structure is similar to that of antimony (Sb) [46,47] and molybdenum disulfide (MoS_2) [48,49]. The layers of Sn and P atoms alternate and form blocks that are seven layers thick, extending along the c-axis. In this arrangement, all P atoms exhibit octahedral

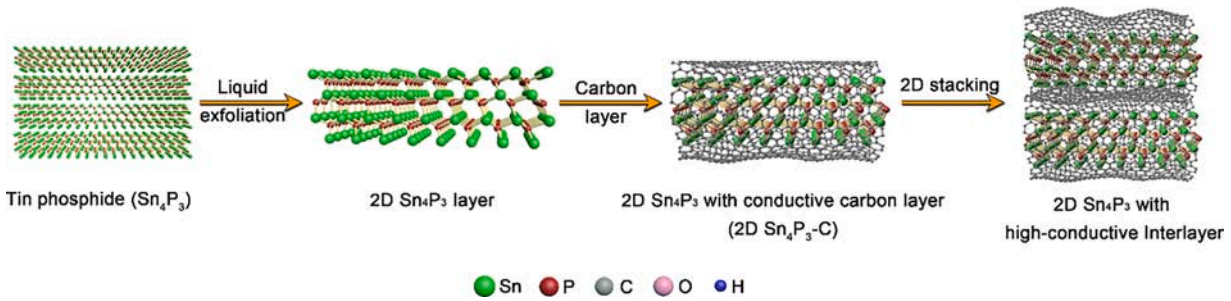

Fig. 1. Schematic illustration of the synthesis route for 2D Sn_4P_3 layer and 2D high-conductive-interlayer Sn_4P_3.

coordination by Sn atoms, while half of the Sn atoms are octahedrally coordinated by P atoms. Due to the weak Van der Waals forces that connect the layers of Sn_4P_3, a liquid-phase exfoliation method can be used to synthesize the 2D Sn_4P_3 layers (Fig. S3). The scanning electron microscope (SEM) images further confirmed that the morphology of Sn_4P_3 bulk where the unique layered structure including cleavage planes

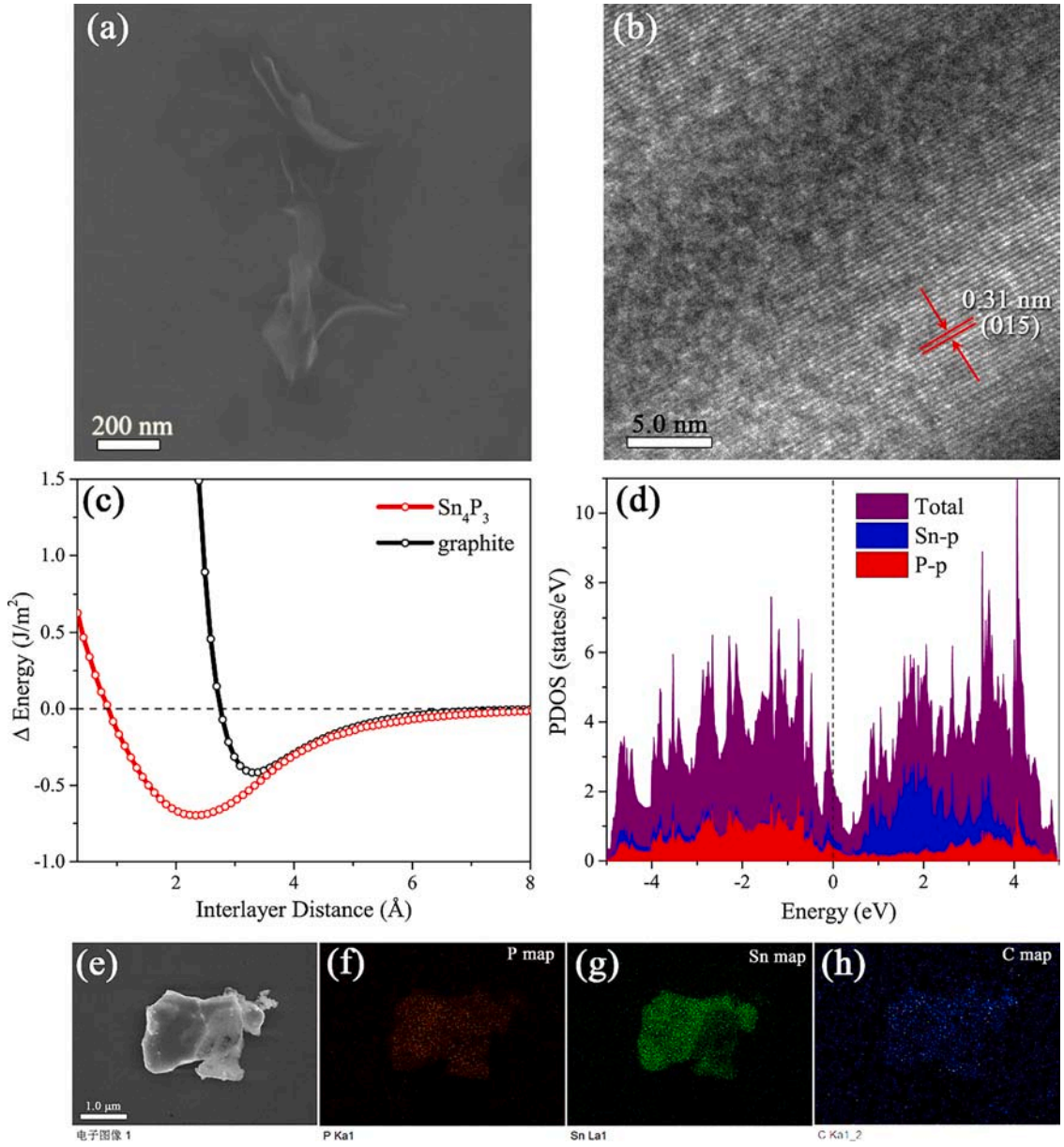

Fig. 2. a) Typical SEM images of 2D Sn_4P_3 layers after sonication in IPA solvent, which demonstrates the ultrathin and flexible features. b) Typical HRTEM image of 2D Sn_4P_3 layers, which reflect the single crystal character. c) The diagram of interlayer binding energy versus interlayer distance belong to Sn_4P_3 and graphite, respectively. d) Partial density of states (PDOS) diagram of monolayer Sn_4P_3, reflecting the metallic feature. e) STEM image of 2D high-conductive interlayer Sn_4P_3 and relevant elemental mapping images of f) P, g) Sn and h) C in the selected region, reflecting the uniformly distribution of elements.

and steps could be directly seen in Fig. S4.

Theoretical analysis as well as experimental results have confirmed that the most efficient exfoliation process for 2D materials occurs when there is a good match between the surface energy of the material and the surface tension of the solvent [46]. In our research, we considered three representative solvents: isopropyl alcohol (IPA), N-methylpyrrolidone (NMP), as well as dimethylformamide (DMF), each with different surface energies. Firstly, the Sn_4P_3 bulk were dispersed in these three solvents with a constant concentration of 2 mg mL^{-1}. During the subsequent sonication process, the solvent molecules gradually penetrated the interlayer spaces of Sn_4P_3, causing the bulk material to expand into monolayer and few-layer nanosheets over time. This sonication process is analogous to the treatment used for Sb, MoS_2, and other 2D materials. After the exfoliation process, the 2D Sn_4P_3 layers were collected by centrifugation at 4000 rpm to remove any unexfoliated samples, followed by multiple washes with ethanol. Our experimental results indicated that IPA was the most effective solvent for exfoliating the Sn_4P_3 bulk into few-layer nanosheets. SEM measurements were conducted for comparison, as shown in Fig. 2a and S5–S7. It is evident that the layers exfoliated using IPA solvent exhibited lateral sizes ranging from 0.2 to 2 μm and displayed ultrathin and flexible characteristics (Fig. 2a), being considerably thinner compared to those exfoliated using NMP and DMF solvents.

To further confirm the structural features, high-resolution transmission electron microscopy (HRTEM) measurements were performed. As demonstrated in Fig. 2b, the 2D Sn_4P_3 layer revealed crystalline lattice fringes with a spacing of 0.31 nm, corresponding to the (015) facets of Sn_4P_3. To determine the precise thickness, atomic force microscopy was conducted, indicating that the Sn_4P_3 layer has a thickness ranging mainly from 1 to 3 nm, corresponding to 1 to 3 layers (Fig. S8). Elemental mapping measurements were employed to analyze the distribution of Sn and P, confirming their uniform dispersion on the 2D Sn_4P_3 layers (Fig. S9).

In order to assess the difficulty and energy requirements for exfoliating Sn_4P_3 bulk into few-layer or monolayer nanosheets, we conducted calculations to determine the binding energy between layers as a function of interlayer distance, and compared it with graphite. The calculated binding energy for graphite layers, as shown in Fig. 2c, was found to be 0.41 J m^{-2}, which corresponds to 68 meV $atom^{-1}$. This value closely matches the experimental value of 62 meV $atom^{-1}$, validating the accuracy of our calculations. Additionally, we found that the binding energy for Sn_4P_3 layers was 0.70 J m^{-2}, which is only 1.7 times larger than that of graphite. This suggests that the exfoliation of few-layer Sn_4P_3 nanosheets from the bulk material can be achieved through liquid exfoliation. Importantly, our theoretical calculations have demonstrated that monolayer Sn_4P_3 exhibits metallic behavior, as indicated by the distribution of PDOS across the Fermi level, as shown in Fig. 2d. This finding is significant, as it represents the first report of a phosphide material exhibiting metallic behavior.

Subsequently, the as-prepared 2D Sn_4P_3 layers were combined with glucose and subjected to hydrothermal treatment at 180 °C for 12 h. This process allowed the glucose molecules to crosslink on the surface of the 2D Sn_4P_3 layers, leading to the formation of Sn_4P_3-glucose stacks. Within these stacks, the 2D Sn_4P_3 layers were weakly interconnected by the glucose polymer. Following the hydrothermal treatment, the samples were subjected to pyrolysis under Ar atmosphere. This process made the formation of unique layer-by-layer structured nanocomposites consisting of 2D Sn_4P_3 layers linked with conductive carbon layers (See experimental section).

To confirm the morphology and composition of the 2D conductive-interlayer Sn_4P_3, SEM and HRTEM measurements were conducted (Fig. S10a and b). The SEM images clearly reveal the unique layer-by-layer structure of the 2D conductive-interlayer Sn_4P_3 nanocomposites. Furthermore, the HRTEM image provides detailed information on the thickness of the carbon layer attached to the surface of 2D conductive-interlayer Sn_4P_3, which measures ~ 1 nm. Additionally, the carbon content in the 2D conductive-interlayer Sn_4P_3 nanocomposites was estimated to be around 11 wt% through acid etching of the Sn_4P_3 component. Besides, the homogeneous elemental dispersions of Sn, P, and C observed in the 2D conductive-interlayer Sn_4P_3 samples further confirm the successful recombination between the 2D Sn_4P_3 layers and interlayer carbon (Fig. 2e–h).

Subsequent XRD, X-ray photoelectron spectroscopy (XPS), and Raman measurements were conducted to gain deep understandings into the crystalline structure as well as compositions of the 2D Sn_4P_3 layers and the 2D high-conductive-interlayer Sn_4P_3 nanocomposites. In Fig. 3a and S11, the XRD spectrums of the exfoliated 2D Sn_4P_3 layers exhibit similar phase peaks to those of Sn_4P_3 bulk, albeit with slightly lower intensities. This observation is consistent with previous findings for exfoliated 2D materials, such as antimonene, [46] graphene, [50,51] and MoS_2 nanosheets [52]. Additionally, the Raman spectra of 2D Sn_4P_3 layers show a weaker and broadened peak compared to Sn_4P_3 bulk (Fig. 3b and Fig. S12), providing further evidence of successful exfoliation. In contrast, the 2D high-conductive-interlayer Sn_4P_3 nanocomposites exhibit even lower intensity in the XRD patterns compared to that of 2D Sn_4P_3 layers, along with the emergence of a new peak at 23.5°, which can be ascribed to the amorphous carbon layer on the surface of 2D conductive-interlayer Sn_4P_3 nanocomposites. Furthermore, two peaks at 1330 and 1600 cm^{-1} in the Raman spectra correspond to the D and G bands of graphite, respectively (Fig. 3b). These observations serve as strong indicators of the successful combination of 2D Sn_4P_3 layers with carbon. To further investigate the hybridization between 2D Sn_4P_3 layers and carbon layers, XPS tests were undertaken. The XPS spectra depicted in Fig. 3c unequivocally validate the presence of Sn, P, C, and O species, with an absence of any extraneous impurities. The Sn 3d spectrum (Fig. 3d) reveals the presence of four distinctive peaks, indicating the coexistence of Sn^{4+} and Sn^{2+} at a ratio of 6.6: 1 within the Sn_4P_3 structure. Additionally, a prominently broad peak is observed at approximately 134 eV in the P 2p spectrum, providing further confirmation of the presence of P—O—C bonds. Moreover, the presence of C—O—P bonds can also be substantiated by analyzing the C 1 s spectrum, which demonstrates the coexistence of C—O—P and C—O—C moieties (Fig. 3e). [30]

To evaluate the electrochemical performance of the 2D high-conductive-interlayer Sn_4P_3 nanocomposites and 2D Sn_4P_3 layers, cyclic voltammetry (CV) measurements were conducted. In Fig. 4a, the first two cycle curves of 2D high-conductive-interlayer Sn_4P_3 nanocomposites were tested in the voltage range of 0.01 ~ 3 V with 0.1 mV s^{-1} are displayed. It can be observed that a broad peak appears at 1.1 V in the initial discharge process, which is attributed to lithium insertion into the 2D conductive-interlayer Sn_4P_3 electrodes. Additionally, two peaks are shown around 0.7 and 0.1 V, corresponding to the reaction of Li with P and Sn, as well as the formation of a SEI film, respectively. The two oxidation peaks centered at 0.5 and 1.0 V in the initial cycle correspond to the decomposition of Li_xSn and Li_3P, respectively. [53,54] The final electrochemical reaction can be represented by the equation: $Sn_4P_3+19Li+19e^- = 3Li_3P+2Li_5Sn_2$. These observations are consistent with the behavior of 2D Sn_4P_3 layer electrode (Fig. S13) and previously reported Sn_4P_3 electrodes.

Furthermore, typical charge-discharge curves of 2D high-conductive-interlayer Sn_4P_3 electrodes are shown in Fig. 4b, exhibiting a platform at around 0.5 V during the charge stage, which is in agreement with the CV results and the behavior of 2D Sn_4P_3 layers (Fig. S14). The initial Coulombic efficiency for 2D high-conductive-interlayer Sn_4P_3 and 2D Sn_4P_3 is calculated as 61.5 % and 35.9 %, respectively. This indicates the high reversibility of 2D conductive-interlayer Sn_4P_3 electrodes should be ascribed to their unique layered structure and high-conductive carbon layers. The reversible capacity and cyclic properties of 2D conductive-interlayer Sn_4P_3, 2D Sn_4P_3 layers, and Sn_4P_3 bulk were evaluated and compared (Fig. 4c). Remarkably, both 2D conductive-interlayer Sn_4P_3 and 2D Sn_4P_3 layer electrodes exhibit similar high reversible capacities of up to 1023 and 986 mAh g^{-1}, respectively, at 74.4 mA g^{-1}. These

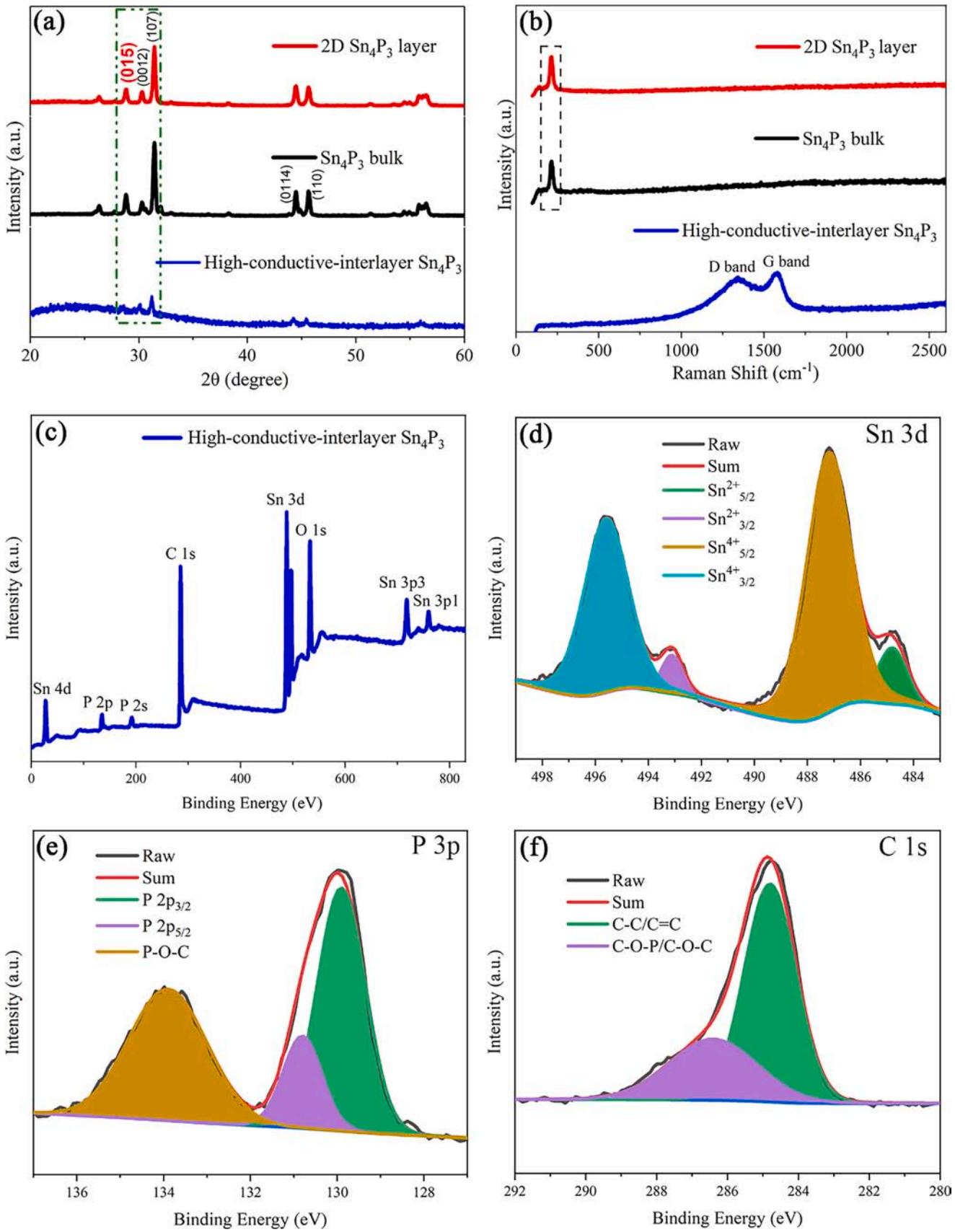

Fig. 3. a) XRD and b) Raman spectra of 2D high-conductive-interlayer Sn_4P_3, 2D Sn_4P_3 layers, and Sn_4P_3 bulk, respectively. c) XPS spectra of 2D high-conductive-interlayer Sn_4P_3. High resolution of d) Sn 3d, e) P 2p, and f) C1s XPS spectra of 2D high-conductive-interlayer Sn_4P_3, respectively.

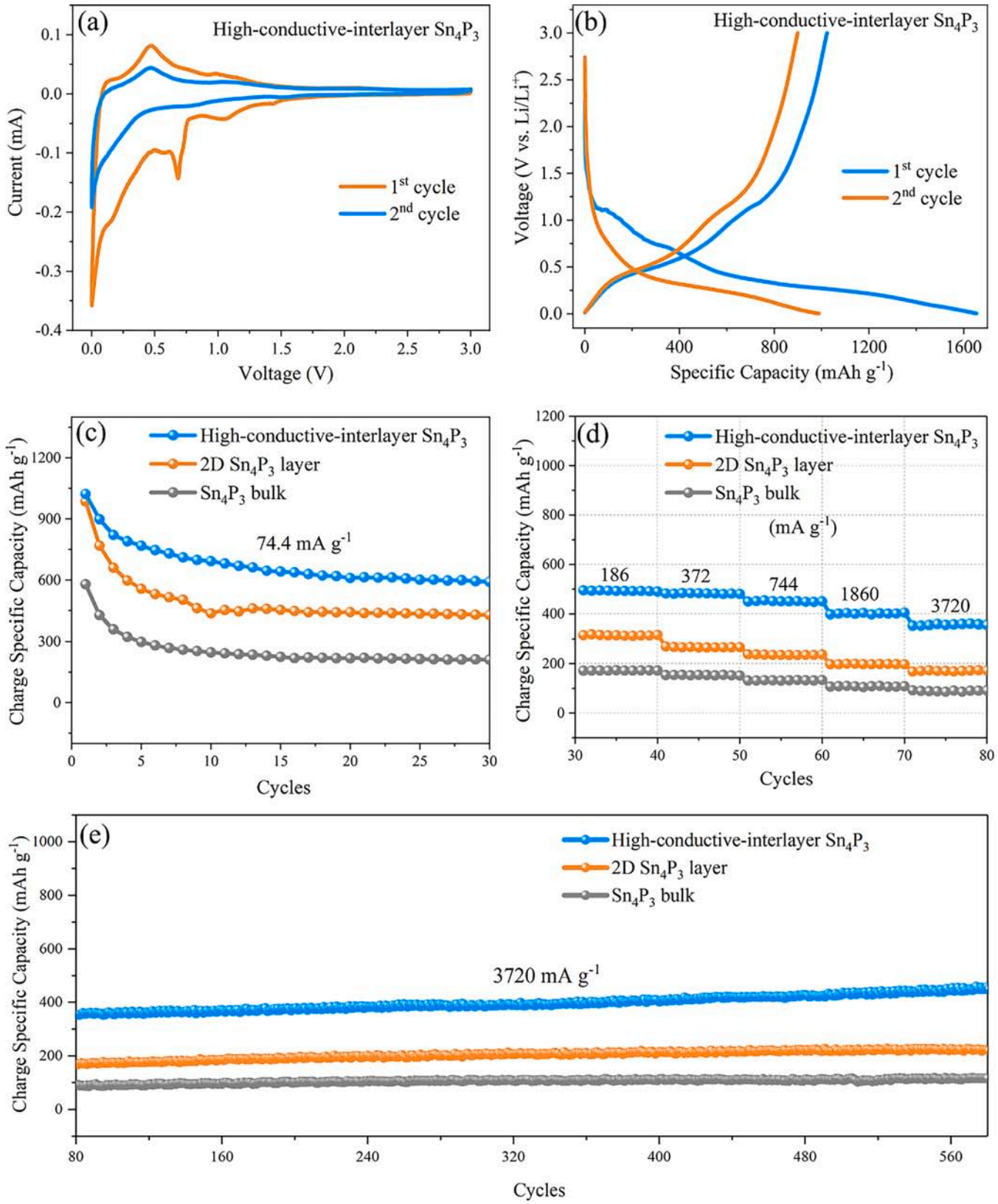

Fig. 4. a) CV and b) Discharge-charge curves of 2D high-conductive-interlayer Sn_4P_3 at the first two cycles, respectively. c) Cyclic performance of 2D high-conductive-interlayer Sn_4P_3, 2D Sn_4P_3 layer, and Sn_4P_3 bulk electrodes at current density of 74.4 mA g^{-1}, respectively. d) Rate performance of 2D high-conductive-interlayer Sn_4P_3, 2D Sn_4P_3 layer, and Sn_4P_3 bulk electrodes at current density of 74.4, 186, 372, 744, 1860, and 3720 mA g^{-1}, respectively. e) Cyclic performance of 2D high-conductive-interlayer Sn_4P_3, 2D Sn_4P_3 layer, and Sn_4P_3 bulk electrodes at high current density (3720 mA g^{-1}), respectively.

values are close to the theoretical capacity of 1230 mAh g^{-1} and significantly higher than that of Sn_4P_3 bulk electrodes. At 30 cycles, the charge capacity of 2D conductive-interlayer Sn_4P_3 electrodes remains at 591 mAh g^{-1}, exceeding that of 2D Sn_4P_3 layer (428 mAh g^{-1}) and Sn_4P_3 bulk (211 mAh g^{-1}) electrodes (Fig. 4c). This suggests that the carbon layer in 2D conductive-interlayer Sn_4P_3 can buffer the significant volume expansion, improve stability with cycling, and increase the capacity compared to 2D Sn_4P_3 layer.

Furthermore, excellent high-rate performance is achieved by 2D conductive-interlayer Sn_4P_3 electrodes. As shown in Fig. 4d, the 2D conductive-interlayer Sn_4P_3 exhibits high reversible capacities of 404 and 365 mAh g^{-1} at high current densities of 1860 and 3720 mA g^{-1}, respectively. In contrast, 2D Sn_4P_3 layer and Sn_4P_3 bulk electrodes only exhibit relatively low capacities of 173 and 85 mAh g^{-1} at the highest current density (3720 mA g^{-1}), which are much lower than that of 2D conductive-interlayer Sn_4P_3 electrodes. To assess the cyclic stability under high current density, the cyclic stability was tested for 580 cycles at 3720 mA g^{-1} (Fig. 4e). Even after 580 cycles, the 2D conductive-interlayer Sn_4P_3 electrodes still maintain an extraordinarily high charge capacity of 446 mAh g^{-1}, which is superior to those of reported Sn_4P_3 electrodes (Table S1). This remarkable long cyclic life further confirms that the unique layer-by-layer structure can effectively buffer the significant volume expansion during the discharge-charge process.

In order to gain insights into the enhanced electrochemical properties of the high-conductive-interlayer Sn_4P_3 electrodes, AC impedance spectra were performed on the 2D conductive-interlayer Sn_4P_3, 2D Sn_4P_3 layer, and Sn_4P_3 bulk electrodes. The Nyquist plot of the 2D conductive-interlayer Sn_4P_3 in Fig. 5a was fitted by a modified Randles equivalent circuit (Fig. S15). The plot comprises a semicircle at high frequencies, signifying the charge-transfer kinetic-controlled region, and a linear segment at low frequencies, representing the mass transfer-controlled Warburg region. The charge-transfer resistance (R_{ct}) obtained from the spectra demonstrates the inhibitory effect on current density. The high-conductive-interlayer Sn_4P_3 electrodes exhibit a very low R_{ct} value of 10.9 Ω, which is significantly lower than that of the 2D Sn_4P_3 layers (14.5 Ω) and Sn_4P_3 bulk (16.6 Ω) (Table S2), indicating the remarkable improvement in electrochemical performance of 2D conductive-interlayer Sn_4P_3 nanocomposites.

Exchange current densities were calculated and summarized in Table S2. The exchange current density of high-conductive-interlayer Sn_4P_3 is 91.8 mA cm^{-2}, higher than that of 2D Sn_4P_3 layers (69 mA cm^{-2}) and Sn_4P_3 bulk (60.3 mA cm^{-2}). Furthermore, the diffusion coefficients of lithium ions in high-conductive-interlayer Sn_4P_3, 2D Sn_4P_3 layer, and Sn_4P_3 bulk were systematically calculated using the equation $D = R^2T^2/2A^2n^4F^4C^2\sigma_w^2$ (for details, see the supporting information) [55]. Notably, the σ_w represents the relationship between Z_{re} and $\omega^{(-1/2)}$ in the low-frequency region (Fig. 5b). High-conductive-interlayer Sn_4P_3 electrodes exhibit an extremely large diffusion coefficient of lithium ions, reaching 5.27×10^{-12} cm^2 s^{-1}, which is ~ 5 and 50 times higher than that of 2D Sn_4P_3 layer (1.04×10^{-12}) and Sn_4P_3 bulk (1.37×10^{-13}), respectively (Table S2). These results indicate that the exfoliation of bulk Sn_4P_3 into few-layer nanosheets significantly improves the electrical conductivity and diffusion coefficient of Li^+. Additionally, the unique layer-by-layer structure formed by carbon and 2D Sn_4P_3 layers facilitates the transfer of electrons and lithium ions, further enhancing the electrochemical performance of high-conductive-interlayer Sn_4P_3 nanocomposites.

4. Conclusion

In conclusion, we successfully synthesized 2D Sn_4P_3 layers with high-conductive-interlayer and unique layer-by-layer structure using a breaking and reconstructing strategy. Besides, the exfoliation of 2D Sn_4P_3 layers was achieved through a liquid-exfoliation method, revealing their metallic properties. Electrochemical performance testing demonstrated that 2D Sn_4P_3 with high-conductive carbon layer exhibited good electrochemical performance, including high charge capacity (1023 mAh g^{-1}), stable cyclic life (580th), and high-rate performance (3720 mA g^{-1}). Furthermore, AC impedance spectroscopy analysis provided insights into the superior electrochemical performance of 2D conductive-interlayer Sn_4P_3 nanocomposites, attributed to the high Li^+ diffusion coefficient. These results highlight the significance of exfoliating Sn_4P_3 into layered structures for enhancing electrochemical performance, with the introduction of a carbon layer further improving stability and ion transport properties. Therefore, the 2D conductive-interlayer Sn_4P_3 nanocomposites hold promise as a candidate material for high-performance LIBs. These findings offer valuable insights for the development of high-performance and sustainable energy storage solutions.

CRediT authorship contribution statement

Jianan Gu: Writing – review & editing, Writing – original draft. **Yanlong Lv:** Writing – review & editing. **Yanhong Wang:** Writing – review & editing. **Lehao Liu:** Writing – review & editing. **Meicheng Li:** Writing – review & editing.

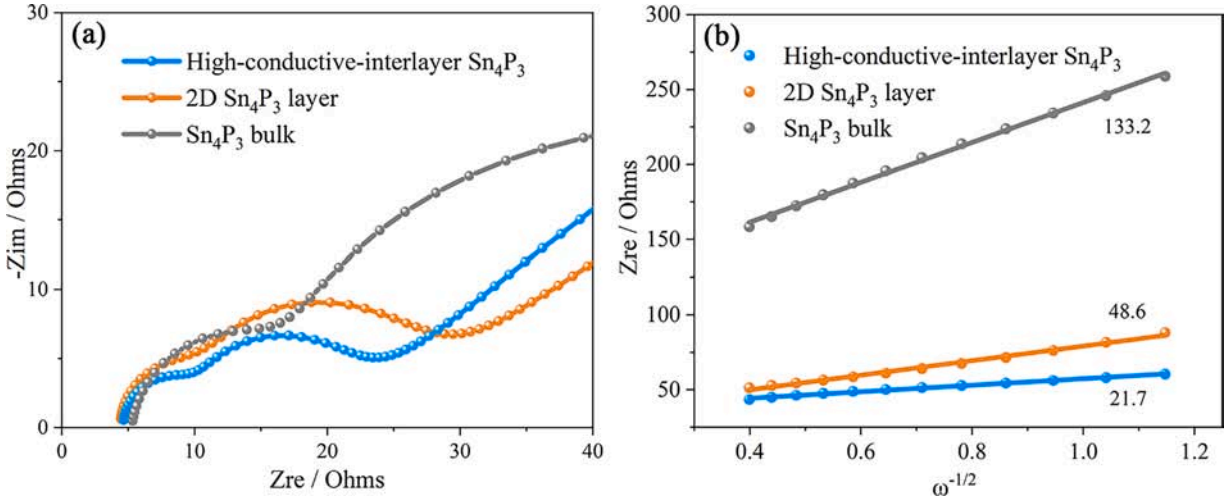

Fig. 5. a) Nyquist plots of high-conductive-interlayer Sn_4P_3, 2D Sn_4P_3 layer, and Sn_4P_3 bulk electrodes, respectively. b) The relationship between Z_{re} and $\omega^{-1/2}$ in the low frequency area.

Declaration of competing interest

The authors declare that they have no known competing financial interests or personal relationships that could have appeared to influence the work reported in this paper.

Data availability

Data will be made available on request.

Supporting Information

Supporting Information is available from the Wiley Online Library or from the author.

Acknowledgments

This work is supported partially by project of State Key Laboratory of Alternate Electrical Power System with Renewable Energy Sources (LAPS21004 and LAPS202114), National Natural Science Foundation of China (Grant nos. 52102203, 52272200, 51972110, 52102245 and 52072121).

Supplementary materials

Supplementary material associated with this article can be found, in the online version, at doi:10.1016/j.electacta.2024.143933.

References

[1] S. Han, B. Wu, H. Wang, P. Wen, L. Zhang, X. Lin, M. Chen, Designing F/P hybrid polymer as ultrastable cationic shielding interphase for high-performance lithium metal batteries, Angew. Chem. Int. Edit. 62 (2023) e202308724.
[2] Q. He, Z. Li, M. Wu, M. Xie, F. Bu, H. Zhang, R. Yu, L. Mai, Y. Zhao, Ultra-uniform and functionalized nano-ion divider for regulating ion distribution toward dendrite-free lithium-metal batteries, Adv. Mater. 35 (2023) 2302418.
[3] Z. Liu, R. Zhang, J. Fu, X. Liu, H. Yang, D. Wang, X. Xu, J. Cao, G. Wen, D. Wang, Mass loading-independent lithium storage of transitional metal compounds achieved by multi-dimensional synergistic nanoarchitecture, Small 19 (2023) 2303019.
[4] J. Wang, J. Zhang, J. Wu, M. Huang, L. Jia, L. Li, Y. Zhang, H. Hu, F. Liu, Q. Guan, M. Liu, H. Adenusi, H. Lin, S. Passerini, Interfacial "single-atom-in-defects" catalysts accelerating Li^+ desolvation kinetics for long-lifespan lithium-metal batteries, Adv. Mater. 35 (2023) 2302828.
[5] D. Xie, M. Zhang, Q. Liu, Y. Lin, A. Yu, Y. Tang, Organic-inorganic conformal extending high-purity metal nanosheets for robust electrochemical lithium-ion storage, Adv. Funct. Mater. 33 (2023) 2306291.
[6] J. Gu, Y. Shi, Z. Du, M. Li, S. Yang, Stress relief in metal anodes: mechanisms and applications, Adv. Energy Mater. 13 (2023) 2302091.
[7] J. Gu, Q. Zhu, Y. Shi, H. Chen, D. Zhang, Z. Du, S. Yang, Single zinc atoms immobilized on MXene ($Ti_3C_2Cl_x$) layers toward dendrite-free lithium metal anodes, ACS Nano 14 (2020) 891–898.
[8] H. Xing, W. Guo, S. Tang, Y. Si, J. Song, Y. Fu, Long-life, high-rate rechargeable lithium batteries based on soluble bis(2-pyrimidyl) disulfide cathode, Angew. Chem. Int. Edit. 62 (2023) e202308561.
[9] L. Yang, Y. Tu, H. Li, W. Zhan, H. Hu, Y. Wei, C. Chen, K. Liu, P. Shao, M. Li, G. Yang, X. Luo, Fluorine-rich supramolecular nano-container crosslinked hydrogel for lithium extraction with super-high capacity and extreme selectivity, Angew. Chem. Int. Edit. 62 (2023) e202308702.
[10] Y. Yi, F. Hai, J. Guo, X. Gao, W. Chen, X. Tian, W. Tang, W. Hua, M. Li, Electrochemical enhancement of lithium-ion diffusion in polypyrrole-modified sulfurized polyacrylonitrile nanotubes for solid-to-solid free-standing lithium-sulfur cathodes, Small 19 (2023) 2303781.
[11] W. Zhang, J. Gao, Y. Huang, G. Xu, Y. Chen, G. Zhao, Y. Lin, Z. Huang, J. Li, Utilizing magnetic-field modulation to efficiently improve the performance of $LiCoO_2$||graphite pouch full batteries, Adv. Funct. Mater. 33 (2023) 2306354.
[12] Y. Zhao, W. Li, Y. Li, T. Qiu, X. Mu, Y. Ma, Y. Zhao, J. Zhang, J. Zhang, Y. Li, H. Tan, 3D covalent polyoxovanadate-organic framework as anode for high-performance lithium-ion batteries, Adv. Funct. Mater. 33 (2023) 2306598.
[13] S. Fan, S. Cui, J. Zhang, J. Rong, W. Wang, X. Xing, Y. Liu, W. Ma, J.-T. Zhao, Two birds with one stone: micro/nanostructured SiO_xC_y composites for stable Li-ion and Li metal anodes, Small 19 (2023) 2304290.
[14] D.-Y. Han, H.B. Son, S.H. Han, C.K. Song, J. Jung, S. Lee, S.S. Choi, W.-J. Song, S. Park, Hierarchical 3D electrode design with high mass loading enabling high-energy-density flexible lithium-ion batteries, Small 19 (2023) 2305416.
[15] P. Hu, W. Chen, Y. Wang, T. Chen, X. Qian, W. Li, J. Chen, J. Fu, Fatigue-free and skin-like supramolecular ion-conductive elastomeric interphases for stable lithium metal batteries, ACS Nano 17 (2023) 16239–16251.
[16] K. Lee, N. Corrigan, C. Boyer, Polymerization induced microphase separation for the fabrication of nanostructured materials, Angew. Chem. Int. Edit. 135 (2023) e202307329.
[17] J. Li, C. Wang, Z. Yu, Y. Chen, L. Wei, MXenes for zinc-based electrochemical energy storage devices, Small (2023) 2304543.
[18] Q. Liu, L. Wang, Fundamentals of electrolyte design for wide-temperature lithium metal batteries, Adv. Energy Mater. 13 (2023) 2301742.
[19] X.-X. Wang, L.-N. Song, L.-J. Zheng, D.-H. Guan, C.-L. Miao, J.-X. Li, J.-Y. Li, J.-J. Xu, Polymers with intrinsic microporosity as solid ion conductors for solid-state lithium batteries, Angew. Chem. Int. Edit. 135 (2023) e202308837.
[20] M. Yang, K. Chen, H. Li, Y. Cao, H. Yang, X. Ai, Molecular adsorption-induced interfacial solvation regulation to stabilize graphite anode in ethylene carbonate-free electrolytes, Adv. Funct. Mater. 33 (2023) 2306828.
[21] W. Zhang, S. Gui, Z. Zhang, W. Li, X. Wang, J. Wei, S. Tu, L. Zhong, W. Yang, H. Ye, Y. Sun, X. Peng, J. Huang, H. Yang, Tight binding and dual encapsulation enabled stable thick silicon/carbon anode with ultrahigh volumetric capacity for lithium storage, Small 19 (2023) 2303864.
[22] T. Zhou, W. Tang, J. Lv, Y. Deng, Q. Liu, L. Zhang, R. Liu, Yolk-shell structured ST@Al_2O_3 enables functional pe separator with enhanced lewis acid sites for high-performance lithium metal batteries, Small 19 (2023) 2303924.
[23] Z. Zhang, L. Feng, H. Liu, L. Wang, S. Wang, Z. Tang, Mo^{6+}–P^{5+} co-doped $Li_2ZnTi_3O_8$ anode for Li-storage in a wide temperature range and applications in LiNi 0.5 $Mn_{1.5}O_4$/$Li_2ZnTi_3O_8$ full cells, Inorg. Chem. Front. 9 (2022) 35–43.
[24] D. Azuma, R. Inada, Characterization of Sn_4P_3 film formed by aerosol deposition for lithium-ion battery anode with liquid electrolyte and solid polymer electrolyte, Thin Solid Films 761 (2022) 139537.
[25] A. Belgibayeva, M. Rakhatkyzy, A. Rakhmetova, G. Kalimuldina, A. Nurpeissova, Z. Bakenov, Synthesis of free-standing tin phosphide/phosphate carbon composite nanofibers as anodes for lithium-ion batteries with improved low-temperature performance, Small 19 (2023) 2304062.
[26] M. Chen, L.-L. Shao, X.-Q. Wang, X. Qian, Z.-Y. Yuan, L.-X. Fang, A.-X. Ding, X.-W. Lv, Y.-N. Wang, Controlled synthesis of highly active nonstoichiometric tin phosphide/carbon composites for electrocatalysis and electrochemical energy storage applications, ACS Sustain. Chem. Eng. 10 (2022) 1482–1498.
[27] Y. Hao, J. Shao, Y. Yuan, X. Li, W. Xiao, H.M.K. Sari, T. Liu, J. Lu, Design of phosphide anodes harvesting superior sodium storage: progress, challenges, and perspectives, Adv. Funct. Mater. 33 (2023) 2212692.
[28] Q. Zhao, D. Zhao, L. Feng, Y. Liu, S. Guo, Sn_4P_3 encapsulated in carbon nanotubes/poly(3,4-ethylenedioxythiophene) as the anode for pseudocapacitive lithium-ion storage, ACS Appl. Energy Mater. 5 (2022) 2412–2420.
[29] G. Ali, M.A.R. Anjum, S. Mehboob, M. Akbar, J.S. Lee, K.Y. Chung, Sulfur-doped molybdenum phosphide as fast dis/charging anode for Li-ion and Na-ion batteries, Int. J. Energy Res. 46 (2022) 8452–8463.
[30] W. Fan, J. Xue, D. Wang, Y. Chen, H. Liu, X. Xia, Sandwich-structured Sn_4P_3@MXene hybrid anodes with high initial coulombic efficiency for high-rate lithium-ion batteries, ACS Appl. Mater. Interfaces 13 (2021) 61055–61066.
[31] Z. Kong, X. Yao, Y. Shao, M. Huang, H. Tu, K. Zhang, Z. Liang, Y. Wu, X. Hao, SnxPy nanoplate/reduced graphene oxide composites as anode materials for lithium-/sodium-ion batteries, ACS Appl. Nano Mater. 4 (2021) 12335–12345.
[32] Q. Liu, C. Liu, Z. Li, Q. Liang, B. Zhu, J. Chai, X. Cheng, P. Zheng, Y. Zheng, Z. Liu, Layered tin phosphide composites as promising anodes for lithium-ion batteries, ACS Appl. Energy Mater. 4 (2021) 11306–11313.
[33] X. Wu, X. Lan, R. Hu, Y. Yao, Y. Yu, M. Zhu, Tin-based anode materials for stable sodium storage: progress and perspective, Adv. Mater. 34 (2022) 2106895.
[34] S. Sun, R. Li, W. Wang, D. Mu, J. Liu, T. Chen, S. Tian, W. Zhu, C. Dai, One-dimensional coaxial cable-like MWCNTs/Sn_4P_3@C as an anode material with long-term durability for lithium ion batteries, Inorg. Chem. Front. 7 (2020) 2651–2659.
[35] M. Wang, G.-M. Weng, G. Yasin, M. Kumar, W. Zhao, A high-performance tin phosphide/carbon composite anode for lithium-ion batteries, Dalton Trans. 49 (2020) 17026–17032.
[36] P. Yadav, W. Malik, P.K. Dwivedi, L.A. Jones, M.V. Shelke, Electrospun nanofibers of tin phosphide ($SnP_{0.94}$) nanoparticles encapsulated in a carbon matrix: a tunable conversion-cum-alloying lithium storage anode, Energy Fuels 34 (2020) 7648–7657.
[37] J. Choi, W.-S. Kim, K.-H. Kim, S.-H. Hong, Sn_4P_3-C nanospheres as high capacitive and ultra-stable anodes for sodium ion and lithium ion batteries, J. Mater. Chem. A 6 (2018) 17437–17443.
[38] A. Chojnacka, X. Pan, P. Jezowski, F. Beguin, High performance hybrid sodium-ion capacitor with tin phosphide used as battery-type negative electrode, Energy Storage Mater. 22 (2019) 200–206.
[39] J. Luis Gomez-Camer, B. Acebedo, N. Ortiz-Vitoriano, I. Monterrubio, M. Galceran, T. Rojo, Unravelling the impact of electrolyte nature on Sn_4P_3/C negative electrodes for Na-ion batteries, J. Mater. Chem. A 7 (2019) 18434–18441.
[40] K. Song, C. Liu, L. Mi, S. Chou, W. Chen, C. Shen, Recent progress on the alloy-based anode for sodium-ion batteries and potassium-ion batteries, Small 17 (2021) 1903194.
[41] Y. Xia, S. Han, Y. Zhu, Y. Liang, M. Gu, Stable cycling of mesoporous Sn_4P_3/SnO_2@C nanosphere anode with high initial coulombic efficiency for Li-ion batteries, Energy Storage Mater. 18 (2019) 125–132.
[42] J. Liu, P. Kopold, C. Wu, P.A. van Aken, J. Maier, Y. Yu, Uniform yolk-shell Sn_4P_3@C nanospheres as high-capacity and cycle-stable anode materials for sodium-ion batteries, Energy Environ. Sci. 8 (2015) 3531–3538.

[43] C. Wu, P. Kopold, P.A. van Aken, J. Maier, Y. Yu, High performance graphene/Ni_2P hybrid anodes for lithium and sodium storage through 3D yolk-shell-like nanostructural design, Adv. Mater. 29 (2017) 1604015.
[44] S. Liu, H. Zhang, L. Xu, L. Ma, X. Hou, High lithium storage performance of Mn-doped Sn_4P_3 nanoparticles, Electrochim. Acta 210 (2016) 888–896.
[45] M. Huang, Y.P. Feng, Stability and electronic properties of Sn_3P_4, Phys. Rev. B 70 (2004) 184116.
[46] J. Gu, Z. Du, C. Zhang, J. Ma, B. Li, S. Yang, Liquid-phase exfoliated metallic antimony nanosheets toward high volumetric sodium storage, Adv. Energy Mater. 7 (2017) 1700447.
[47] J. Gu, J. Ma, Z. Du, C. Zhang, S. Yang, Few-layer tin-antimony nanosheets: a novel 2D alloy for superior lithium storage, Chem. Comm. 55 (2019) 3975–3978.
[48] D. Chiappe, E. Scalise, E. Cinquanta, C. Grazianetti, B. van den Broek, M. Fanciulli, M. Houssa, A. Molle, Two-dimensional Si nanosheets with local hexagonal structure on a MoS_2 surface, Adv. Mater. 26 (2014) 2096–2101.
[49] H. Tang, J. Wang, H. Yin, H. Zhao, D. Wang, Z. Tang, Growth of polypyrrole ultrathin films on MoS_2 monolayers as high-performance supercapacitor electrodes, Adv. Mater. 27 (2015) 1117–1123.
[50] M. Cai, R.A. Outlaw, R.A. Quinlan, D. Premathilake, S.M. Butler, J.R. Miller, Fast response, vertically oriented graphene nanosheet electric double layer capacitors synthesized from C_2H_2, ACS Nano 8 (2014) 5873–5882.
[51] Y. Guo, S. Guo, J. Ren, Y. Zhai, S. Dong, E. Wang, Cyclodextrin functionalized graphene nanosheets with high supramolecular recognition capability: synthesis and host-guest inclusion for enhanced electrochemical performance, ACS Nano 4 (2010) 4001–4010.
[52] H. Li, J. Wu, Z. Yin, H. Zhang, Preparation and applications of mechanically exfoliated single-layer and multi layer MoS_2 and WSe_2 nanosheets, Acc. Chem. Res. 47 (2014) 1067–1075.
[53] Z. Liu, X. Wang, Z. Wu, S. Yang, S. Yang, S. Chen, X. Wu, X. Chang, P. Yang, J. Zheng, X. Li, Ultrafine Sn_4P_3 nanocrystals from chloride reduction on mechanically activated Na surface for sodium/lithium ion batteries, Nano Res. 13 (2020) 3157–3164.
[54] Z.T. Wondimkun, T.T. Beyene, M.A. Weret, N.A. Sahalie, C.-J. Huang, B. Thirumalraj, B.A. Jote, D. Wang, W.-N. Su, C.-H. Wang, G. Brunklaus, M. Winter, B.-J. Hwang, Binder-free ultra-thin graphene oxide as an artificial solid electrolyte interphase for anode-free rechargeable lithium metal batteries, J. Power Sources 450 (2020) 227589.
[55] J. Gu, Z. Du, C. Zhang, S. Yang, Pyridinic nitrogen-enriched carbon nanogears with thin teeth for superior lithium storage, Adv. Energy Mater. 6 (2016) 1600917.